CrossMark

Al₂O₃/Al Cermets by Plasma Spraying: Optical Response of Experimental and Numerically Represented Materials

D. Toru, R. Echegut, A. Quet, D. De Sousa Meneses, L. del Campo, H. Piombini, P. Echegut, and L. Bianchi

Optical properties of plasma-sprayed coatings and numerically represented samples were studied at wavelengths ranging from visible to mid-infrared. The paper focuses on Al₂O₃ and Al₂O₃/Al cermet coatings with different metal concentrations. Microstructure and composition of the samples were characterized in order to explain their optical response that is highly dependent on volume and/or surface scattering as a function of the wavelength range. 2D scanning electron microscopy and 3D x-ray microtomography images were exploited to get statistical data in order to numerically represent simplified samples from the complex microstructure of plasma-sprayed coatings. A Monte Carlo ray-tracing model, based on geometrical optical laws, was then applied to reproduce experimental trends of the acquired optical spectra. Good agreement with the experimental data was obtained.

1. Introduction

Plasma-sprayed coatings are decidedly heterogeneous materials. They indeed exhibit a complex microstructure including a multiscale and multishape porosity, as well as rough surfaces. Such characteristics are known to influence strongly the optical behavior of materials. Previous studies on porous transparent oxides have shown that optical properties are both driven by the complex optical index of the material depending on the composition and by heterogeneities such as porosity, roughness, grain boundaries, and second phases leading to radiation scattering (Ref 1).

Plasma spraying stands out by its high versatility and the diversity of materials that can be processed. The process has found many applications to deposit protective layers against wear, erosion, high temperature, or corrosion attack. Optical properties of such coatings have hardly been investigated. The current state-of-the-art related to optical properties of plasma-sprayed coatings deals mainly with heat transport by radiative transfer in plasma-sprayed thermal barrier coatings such as yttria-stabilized zirconia (Ref 2-5) or zirconates (Ref 6). Other experimental studies were also conducted in plasma-sprayed alumina materials for reflective mirrors (Ref 7) or in selective solar absorber coatings for energy applications (Ref 8, 9). Regarding numerical approach, two-flux (Kubelka-Munk) or four-flux methodologies, allowing the determination of the absorption and scattering coefficients from experimental data, were among methods used to predict optical properties of TBC coatings (Ref 3, 5, 6). Other methods exist to compute the optical response of such scattering media, including Mie theory (Ref 10), the transition matrix null-field method, the discrete-dipole approximation, the finite-element method, or the finite-difference time-domain method (Ref 11). Ray-tracing, or the geometric optics approximation, provides also a promising method for the computation of the hemispherical spectral reflectance and transmittance in porous media (Ref 12, 13). Each method presents advantages and disadvantages such as rapid or lengthy computation time, and inclusion of spherically or arbitrary shaped particles.

Besides microstructure, optical properties of materials are strongly influenced by composition (Ref 14). There are advantages that can be derived from a composite system such as the tailoring of the material properties between the different components. A particular case of composite coatings is constituted by cermets (ceramic-metal materials) which possess properties of both ceramics and metals. By varying the amount of each material, cermets may be designed to obtain desired reflectance or emittance. Indeed, in the visible, near and mid-infrared (NIR and MIR), metals and dielectric oxides have very different optical properties.

To extend the knowledge of the optical properties of plasma-sprayed coatings and promote the use of this process regarding to optical functional properties, this

D. Toru, A. Quet, H. Piombini, and **L. Bianchi**, CEA DAM, Le Ripault, Monts, France; and **R. Echegut, D. De Sousa Meneses, L. del Campo,** and **P. Echegut**, CNRS-CEMHTI UPR 3079, Orléans, France. Contact e-mails: aurelie.quet@cea.fr. and luc.bianchi@cea.fr.

paper focuses on the optical response of both experimental and numerically represented samples. Aluminum and alumina were selected as materials. Taking into account plasma-sprayed material thicknesses, aluminum is opaque and highly reflective. Alumina is semitransparent from the visible to NIR, and opaque in the MIR spectral range. Alumina shows no darkening linked to loss of oxygen during its treatment into the plasma jet that may affect its optical properties. This implies that one does not have to resort to annealing to compare the optical properties. Besides, in case of a slight oxidation of aluminum powder, the resulting oxide would be alumina.

Directional-hemispherical reflectances and transmittances were measured at wavelengths from 0.4 to 16 μm on several experimentally plasma-sprayed samples. The understanding of the optical behavior requires accurate characterization of the two main parameters affecting it: aluminum phases and porosity. Detailed results were recently published elsewhere (Ref 14). Simplified numerically represented materials were built from data resulting from the different characterization methods and were then used to simulate optical properties of plasma-sprayed coatings by a 3D Monte Carlo ray-tracing approach. The paper presents the results related to Al_2O_3 prior to that of Al_2O_3/Al cermet coatings.

2. Materials and Methods

2.1 Experimental Samples

2-mm-thick coatings were produced by plasma spraying on grit-blasted aluminum substrates. Fused and crushed alumina from H.C. Starck (+22-45 μm, Amperit 740.1), and aluminum from Oerlikon Metco (+22-45 μm, 54NS-1) were used as feedstock powders (Fig. 1). Plasma spraying was performed with a F4VB torch (Oerlikon Metco) working under air at atmospheric pressure. Metal and ceramic powders were fed radially and separately into the plasma jet. The two powders were injected downstream of the torch nozzle exit. The injector of the aluminum powder was positioned farther than that of the alumina powder into the plasma jet due to the very different thermal properties of the two materials. The plasma parameters used are listed in Table 1.
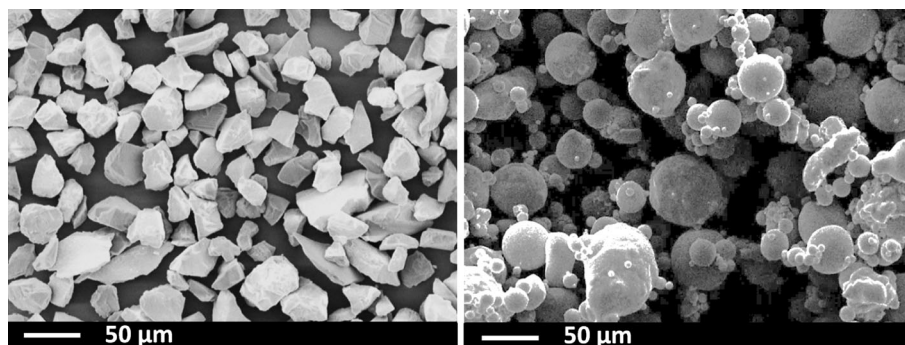
An Ar-He-H_2 mixture was used as plasma gas. Both injections of Al_2O_3 and Al carrier gas were adapted to optimize the particle penetration into the plasma jet. The quantity of metal was adjusted from 0 to 100 wt.%, leading to seven different types of coatings. Coatings were removed from substrates to obtain freestanding samples for characterization purposes.

2.2 Characterization of Coatings

Coating total void content was estimated by image analysis performed thanks to the ImageJ software (resolution 0.09 μm/pixel) on 10 cross-sectional images of coatings obtained by scanning electron microscopy (SEM, LEO 440). Alumina sample images were acquired by x-ray synchroton microtomography (XMT, ESRF, beamline ID19, Grenoble), with a 0.28 μm/pixel resolution. 3D reconstruction was made with the ImageJ software. Arithmetic surface roughness of the coatings was measured with a Perthometer S2. Crystalline structure was investigated with a D5000 x-ray diffractometer (XRD, Siemens A.G.) using Cu Kα radiation.

Room temperature directional-hemispherical reflectances and transmittances were collected from the visible wavelengths up to 16 μm with two different spectrometers (Cary 5000 and Bruker IFS66). An integrating sphere was used to fully collect hemispherical radiation scattered by the sample.

In order to establish a correlation between composition and optical behavior, accurate quantification of the proportion of aluminum in cermets was needed. A mean value was obtained by four different methods, based on image analysis (SEM and optical microscopy), Archimedes' method, and quantitative XRD measurements by standard additions (spiking).

Table 1 Spray parameters

Ar gas flow rate, slpm	20
He gas flow rate, slpm	30
H_2 gas flow rate, slpm	10
Current intensity, A	500
Gun power, kW	35
Spraying distance, mm	140
Distance between Al_2O_3 and Al injectors	30
Al_2O_3 carrier gas flow rate (Ar), slpm	2.7
Al carrier gas flow rate (Ar), slpm	3.5

Fig. 1 SEM images of feedstock powders: alumina (left) and aluminum (right)

2.3 Numerically Represented Samples

In order to simulate optical properties, 3D numerically represented samples were built from statistical data resulting from 2D and 3D image analysis. Statistical data on pore dimensions were extracted from XMT 3D alumina images. Unfortunately, it was not possible to acquire from XMT images data on aluminum splats due to lack of contrast between aluminum and alumina. Therefore, cross-sectional SEM images and coating surface SEM images of the coatings were exploited to access diameters and thicknesses of aluminum splats. Both pore and aluminum splat size distributions were fitted using log-normal laws.

2.4 Numerical Simulation of Optical Properties

The stochastic ray-tracing method was used to simulate optical properties of the materials. The main assumption underlying ray-tracing relies on the application of geometrical optic laws. As a result, the code is based on Snell's law, the Fresnel equations, and Beer-Lambert's law. It requires input data such as a numerically represented sample and complex optical indices which were extracted from the literature (Ref 15, 16).

The ray-tracing method consists of generating a large number of incident rays from an incident beam source and launching them toward the numerically represented material. The optical properties are simulated by the use of trajectories of this statistically large number of rays. Each ray was associated with an intensity equal to 1. Inside the sample, when a ray encounters an interface, its new direction was defined according to Snell's law. At each change of medium, directional spectral reflectivity and transmitivity were governed by Fresnel's formulae. All along its path through Al and Al_2O_3, the ray is absorbed following Beer-Lambert's law. Upon completion of the procedure, the number of reflected, transmitted and absorbed rays was counted. The directional-hemispherical reflectance is obtained by the ratio of the number of backscattered rays to the total number of incident beam rays. The directional-hemispherical transmittance is given by transmitted rays and the emittance can be deduced by Kirchhoff's law.

3. Results and Discussion

3.1 Composition and Microstructure

Figure 2 and 3 show cross-sectional SEM images illustrating the microstructure of as-sprayed alumina and cermet coatings. The alumina coating exhibits spherical pores, interlamellar voids, and intralamellar microcracks typical of plasma-sprayed ceramic coatings. In cermet coating cross sections, lighter zones represent aluminum phases, while the darkest ones correspond to alumina phases. Aluminum particles are mostly spread and randomly distributed through the different coatings.

Figure 4 shows cermet surface morphologies. SEM images in backscattering mode highlighted aluminum splats showing a fragmented morphology.

Roughness and total void content of coatings evolve with the increasing Al content (Fig. 5): roughness slightly increases from 7 to 13%; porosity rate decreases with the addition of aluminum. Porosity of pure aluminum coatings appears relatively high with 13% due to the Al injector position downstream in the plasma jet.

The starting alumina powder was entirely composed of α-alumina. Rapid cooling rate of molten particles leads to the formation of the γ-phase. Quantification of the amount of each crystalline phase, by the spiking XRD method, showed that 96% of the alumina coating is composed of γ-alumina, and the residual 4% can be attributed to unmelted α-alumina particles.

3.2 Optical Properties of Coatings

Experimental optical properties are discussed in more detail in Ref 14. Figure 6 and 7 show, respectively, the evolution of refractive index, n, and extinction coefficient, k, for monocrystalline alumina, and the measured directional-hemispherical reflectance of the as-sprayed, polished, and annealed alumina coatings in the wavelength range from 0.4 to 16 μm.

At short wavelengths, interactions between electromagnetic radiation and material microstructure explain the high value of reflectance of alumina plasma-sprayed coating (Ref 17). The optical response results from the sample volume. Nevertheless, despite the very low extinction coefficient of alumina, the plasma-sprayed
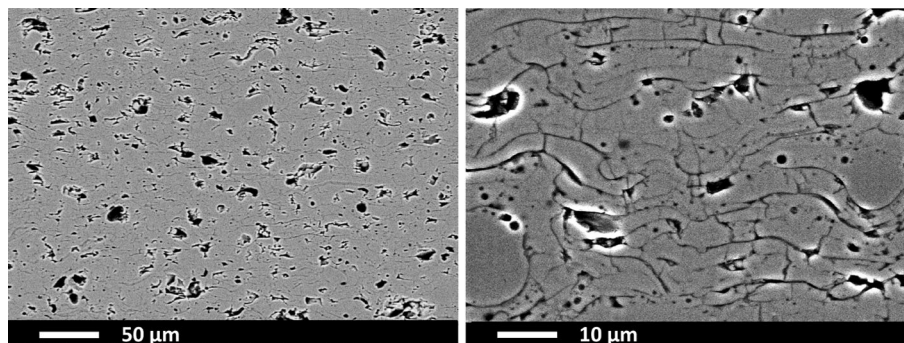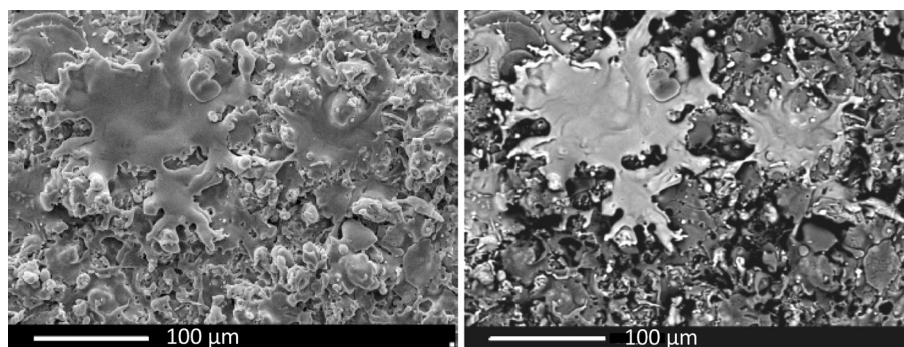

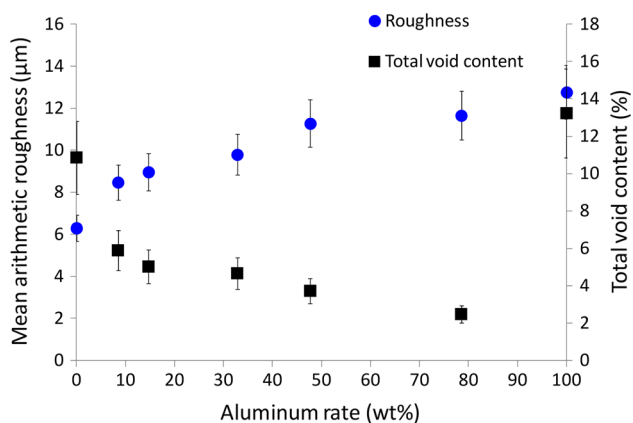**Fig. 2** Cross-sectional SEM images of alumina coatings
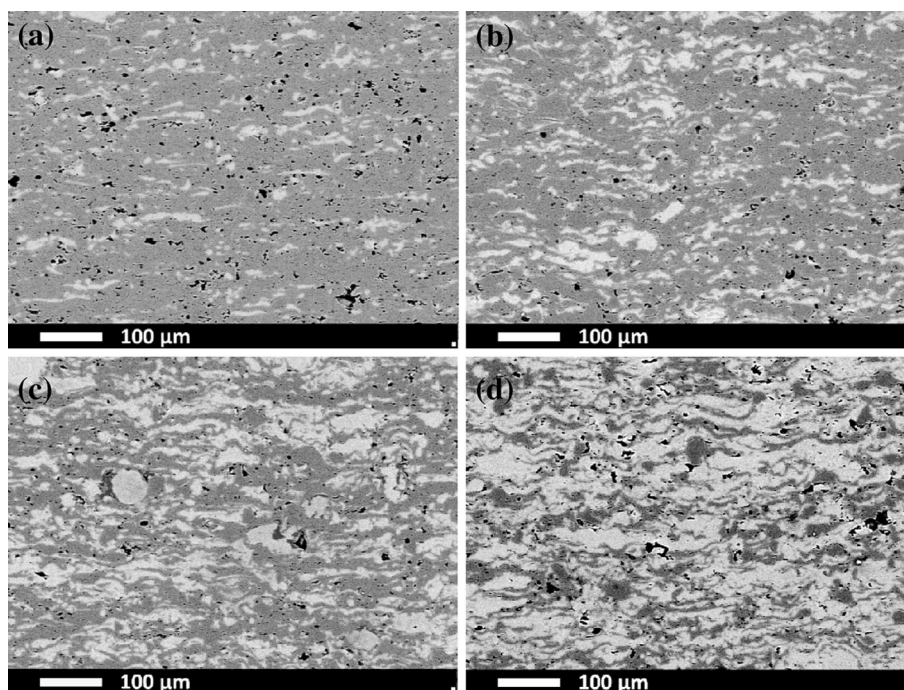
Fig. 3 Cross-sectional SEM images of cermet coatings: (a) Al$_2$O$_3$-10 wt.% Al, (b) Al$_2$O$_3$-20 wt.% Al, (c) Al$_2$O$_3$-33 wt.% Al, (d) Al$_2$O$_3$-50 wt.% Al
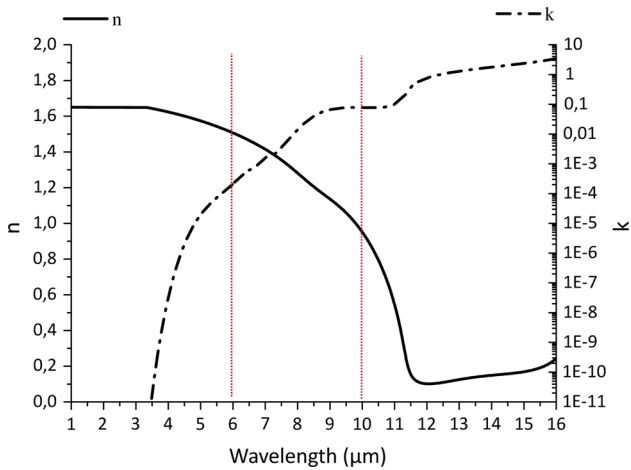

Fig. 4 Secondary (left) and backscattered-electron (right) SEM images of cermet coating surfaces: Al$_2$O$_3$-20 wt.% Al
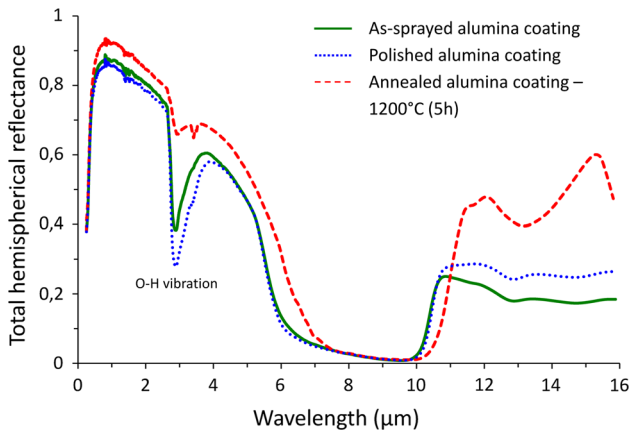

Fig. 5 Total void content measured by image analysis and roughness of as-sprayed coatings

alumina coating shows no transmittance, because of its 2 mm thickness and volume scattering induced by pores. Therefore, according to Kirchhoff's law, a part of the radiation is absorbed, possibly by impurities such as transition metal oxides (Ref 1). Hydroxyl groups or moisture adsorbed by alumina produced a significant absorption peak noticed at 3 μm wavelength. Annealing of alumina coatings for 5 h at 1200 °C in an oxidizing atmosphere reduced the OH content in the coating leading to the reduction of O-H vibration peak. Between 1 and 6 μm, reflectance decreases. On the one hand, the size of the scattering pores decreases compared with the wavelength, leading to the reduction of backscattering. On the other hand, the extinction coefficient rises with the wavelength (Fig. 6).

From 6 to 10 μm, reflectance decreases to zero because the alumina absorption coefficient rises (Fig. 6), turning
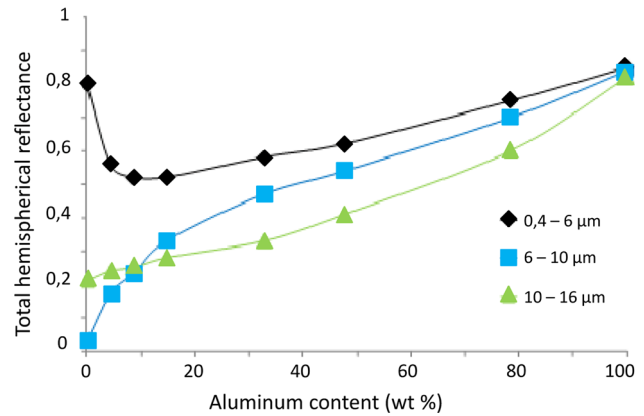
Fig. 6 Refractive index, *n*, and extinction coefficient, *k*, for monocrystalline alumina

Fig. 7 Reflectance spectra of as-sprayed, polished and annealed (1200 °C, 5 h) alumina coatings with a thickness of 2 mm

Fig. 8 Reflectance values of plasma-sprayed cermet coatings with the increasing aluminum content for each of the three wavelength ranges characteristic of alumina optical behavior
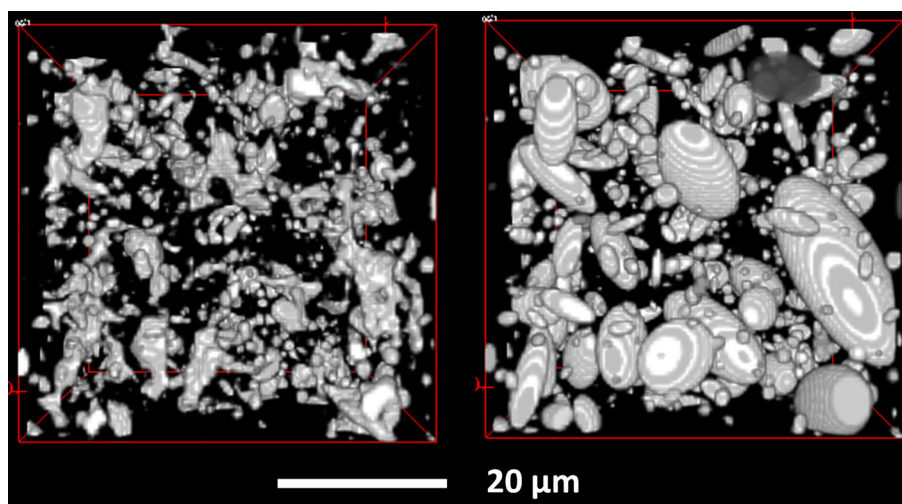
Regarding aluminum coatings, reflectance is high, about 80%, on the entire considered wavelength range. It is lower than that of homogeneous and polished metal because of the 10 μm arithmetic roughness.

Optical properties of cermet coatings were studied through the average reflectance values obtained for the following three spectral domain wavelengths ranging from (a) 0.4 to 6 μm, (b) 6 to 10 μm, and (c) 10 to 16 μm, corresponding, respectively, to regions of low, intermediate, and high absorption coefficients of alumina (Fig. 6).
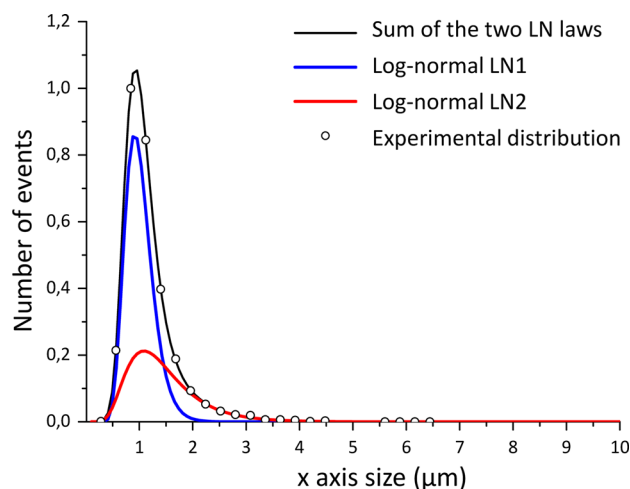
The composition dependence of the average hemispherical reflectance of the as-sprayed coatings is presented in Fig. 8. The optical response of cermet coatings is between those of aluminum and of alumina. Reflectance shows strong composition dependence and its evolution is different in the three spectral domains.

From 0.4 to 6 μm, aluminum has a strong extinction coefficient, while alumina exhibits a very low extinction coefficient, leading to penetration of radiation into the coating. For low amounts of aluminum, reflectance decreases compared to that of alumina. This composition-dependent trend originates from the absorption by a low density of aluminum splats in the alumina matrix. The aluminum lamellae dispersed within the sample modify the photon path, leading to a higher absorption and to a significant reduction of reflectance. In this composition range, volumetric effects prevail over surface effects. When the aluminum content becomes high enough, surface effects prevail over volumetric effects, and reflectance rises toward the 100 wt.% aluminum coating level. As a consequence, cermet reflectance results from the addition of surface and volumetric contributions.

From 6 to 10 μm, aluminum and alumina show, respectively, a high and an intermediate absorption coefficient. The optical behavior is roughly the same in this wavelength range as in the 0.4-6 μm spectral range, except that the volumetric effects do not act in the same way due to the higher absorption coefficient of alumina, inducing a lower reflectance. Reflectance appears to be directly linked to the amount of aluminum: the higher the aluminum content is, the higher the reflected radiation.

the coating into an opaque and absorbent surface. The penetration depth of the radiation decreases from hundreds of micrometers to 20 μm with increasing wavelength. At 10 μm, reflectivity is close to zero, as predicted by Fresnel's law using a value of 1 for the refractive index and a negligible extinction coefficient.

From 10 to 16 μm, the plasma-sprayed alumina coating exhibits 20% reflectance. Due to the high absorption coefficient, radiation interacts only with the sample surface as highlighted by polishing that affects the optical behavior only in this wavelength range. The difference with monocrystalline α-alumina, which reflects about 80% of radiation in this spectral range (Ref 15), is related to both different crystallographic structure and surface roughness. Indeed, γ-alumina is less reflective than α-alumina as suggested by the fact that annealing of the as-sprayed coating leads to reformation of the α-phase with a significant increase of reflectance (Fig. 7). Besides, with an arithmetic roughness of about 6 μm, a large part of the radiation is absorbed due to trapping and multiple reflections of photons on the asperities of the surface.
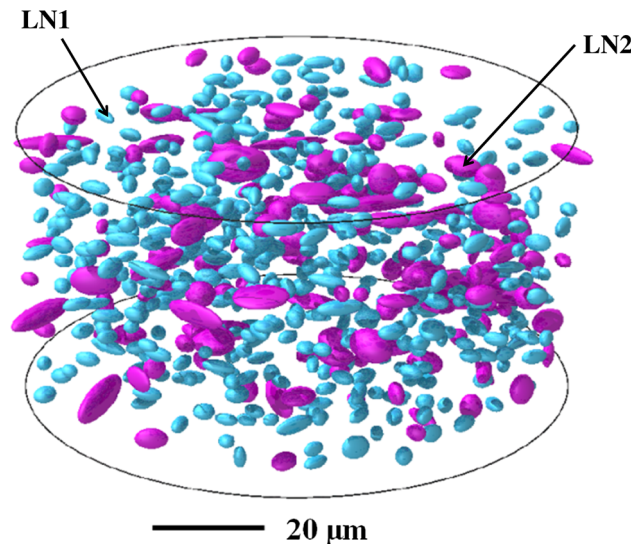
Fig. 9 XMT analysis of plasma-sprayed alumina coatings

Fig. 10 Porosity—Experimental and fitted size distributions of the long axis (*x*-axis) of the ellipsoidal pores
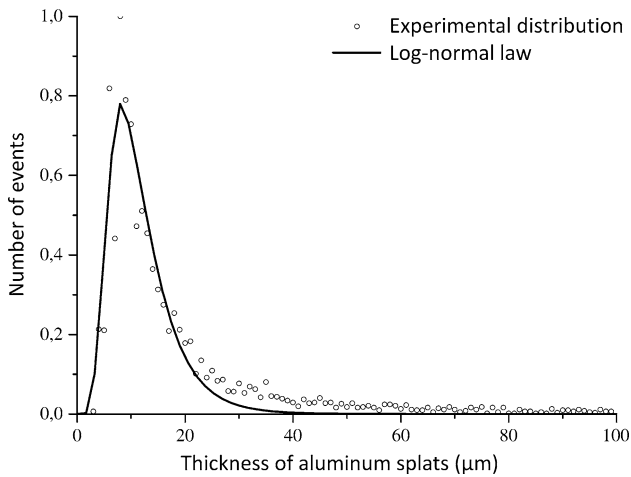

Fig. 11 Part of numerically represented porous alumina sample (blue: pore distribution according to the first log-normal law LN1, purple: pore distribution according to the second log-normal law LN2)

From 10 to 16 μm, both alumina and aluminum have strong extinction coefficients, leading to a very small penetration depth of the radiation into the coating. The optical response results essentially from the roughness leading to surface scattering and from the composition of the sample surface.

3.3 Numerically Represented Samples

A 3D image of an alumina coating obtained by XMT is shown in Fig. 9. Alumina is displayed as being transparent. Complex and tortuous porous microstructure is highlighted, but crack network and intralamellar voids are not visible due to resolution limitations (Ref 18). Therefore, the total void content of 6% appears to be lower than that of 9 to 10% estimated from 2D SEM image analysis.

XMT images, allowing the extraction of three-dimensional parameters, were used to produce numerically represented alumina samples.

The voids within the coating were assumed to be ellipsoidal in shape and were fitted with ellipsoids using the ImageJ software (Fig. 9). Size distributions of equatorial radii (along the *x*- and *y*-axes) and polar radius (along the *z*-axis) of ellipsoids were then fitted with a sum of two log-normal laws, LN1 and LN2 (Fig. 10). 3D numerically represented alumina samples were obtained as shown in Fig. 11.

A numerically represented cermet sample is represented in Fig. 13. It was built assuming the same pore size distribution than that of alumina samples and from aluminum splat data extracted from cross-sectional and top-

Fig. 12 Aluminum splats—Experimental and fitted size distributions of thicknesses
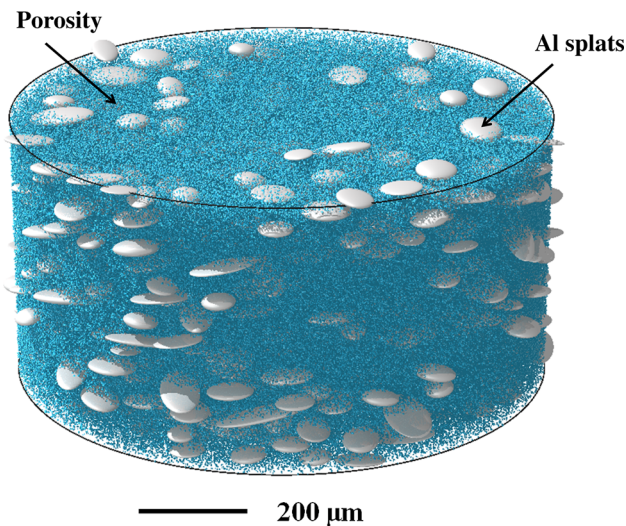

**Fig. 13** Part of numerically represented porous cermet sample (gray: aluminum splats, blue: porosity)

view SEM images (Fig. 12). Aluminum splats were assumed to be not connected together. Aluminum diameters smaller than 20 µm were not taken into account, due to roughness that restricts the quality of SEM pictures.

3.4 Modeling of Optical Properties

Simulated reflectance shown in Fig. 14 and 15 were obtained by launching 10^5 rays onto, respectively, alumina and cermet numerically represented samples. The dimensions of the cylindrically shaped samples were 50 mm diameter by 2 mm thickness. Total void content was 9%. The simulated reflectances were compared with the measured values at wavelengths from 1 to 10 µm; the optical behavior at higher wavelengths is being driven by surface effects, 3D samples are not required.
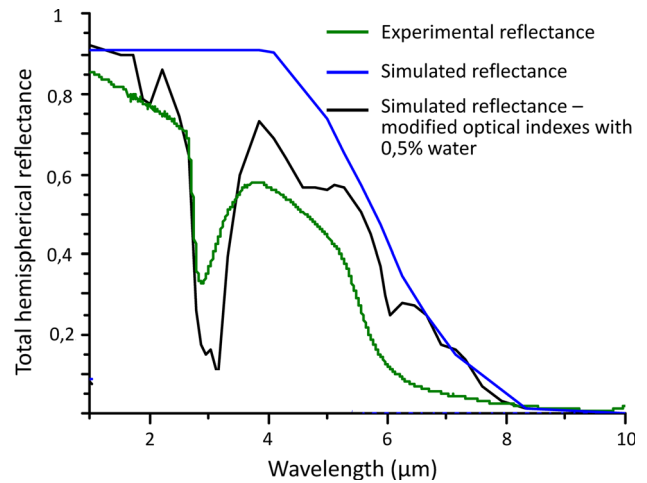
Fig. 14 Comparison between experimental and simulated optical properties of alumina coatings—Simulated curves were obtained with monocrystalline alumina optical indices (blue curve), and monocrystalline alumina optical indices modified with 0.5 vol.% water (black curve) (Color figure online)
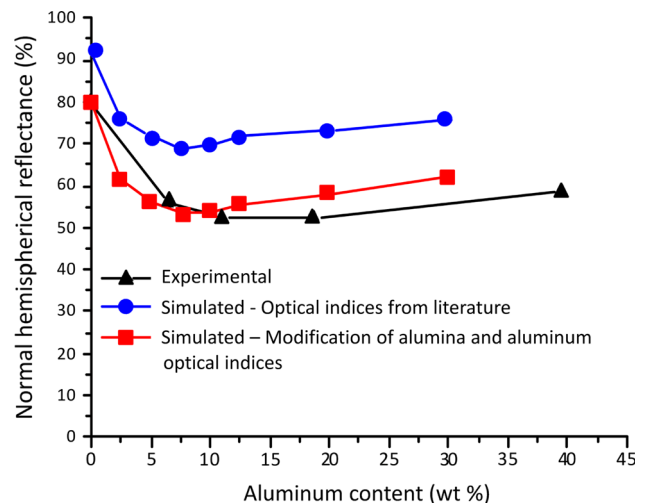
Fig. 15 Comparison between experimental and simulated cermet optical properties at a wavelength of 2 µm

Regarding alumina coatings, the high level of reflectance was reproduced as well as the experimental trend (Fig. 14). Discrepancies between experimental and simulated reflectances can be explained by overestimating backscattering independent of the size of the scattered pores versus the wavelength and to the optical indices used. Indeed, the optical indices of monocrystalline alumina do not take into account absorption of O-H groups or impurities that might lead to increase of the absorption coefficient of alumina (Ref 1). After modifying these optical indices by adding 0.5% of water, the absorption peak at 3 µm appears.

Experimental optical trend of cermets was also obtained with ray-tracing (Fig. 15). Optical indices can be adjusted to decrease the difference to experimental reflectance values. Absorption coefficients of both alumina and aluminum were increased taking into account, respectively, impurities such as iron oxide and splat texture, different to that of the polished surface.

The validity of geometrical optical laws used in the ray-tracing code implies that the wavelength of light is short compared to the object scales. If this assumption remains valid for aluminum splats, it is debatable for pore size distribution, in the same range as the wavelength of the radiation. The main consequence is the failure to reproduce the reflectance decrease between 1 and 4 μm. Nevertheless, ray-tracing turned out to be relatively easy to use, able to work with large sample size (a few mm^3) in a required computation time of a few minutes, and reliable to reproduce optical behavior of plasma-sprayed coating.

4. Conclusions

Optical properties of plasma-sprayed coatings and numerically represented samples were studied at wavelengths from the visible to MIR range. The optical response of the coatings results from the weighted response of contributions of light scattering due to surface roughness and volumetric heterogeneity, such as porosity. Simplified numerically represented materials were built from data resulting from 2D and 3D images and were used to simulate optical properties of plasma-sprayed coatings by the Monte Carlo ray-tracing method. Even though two of the three main porous components of plasma-sprayed coating, i.e., intralamellar cracks and intersplat lamellar pores, cannot be reproduced by XMT analysis and, hence, are not considered in numerically represented samples, good agreement with experimental trends was shown. Therefore, ray-tracing appears to be well suited to predict reflectance and transmittance of plasma-sprayed coatings. This makes eligible the Monte Carlo ray-tracing approach to drive the design of plasma-sprayed coating in order to obtain desired performances. Besides, knowing assumptions and their impact on the computed results, it could be an effective tool to predict radiative transport through thermal barrier coatings or to consider the influence of the microstructure parameters such as porosity, shape, size, and orientation of splats on the optical properties.

Acknowledgments

References

1. J.G.J. Peelen, ''Alumina: Sintering and Optical Properties'', Thesis, 1977, p. 101
2. A. Stuke, H. Kassner, J.-L. Marqués, R. Vassen, D. Stöver, and R. Carius, Suspension and Air Plasma-Sprayed Ceramic Thermal Barrier Coatings with High Infrared Reflectance, *Int. J. Appl. Ceram. Technol.*, 2012, **9**(3), p 561-574
3. J.I. Eldridge and C.M. Spuckler, Determination of Scattering and Absorption Coefficients for Plasma-Sprayed Yttria-Stabilized Zirconia Thermal Barrier Coatings, *J. Am. Ceram. Soc.*, 2008, **91**(5), p 1603-1611
4. L. del Campo, D. De Sousa Meneses, K. Wittmann-Ténèze, A. Bacciochini, A. Denoirjean, and P. Echegut, Effect of Porosity on the Infrared Radiative Properties of Plasma-Sprayed Yttria-Stabilized Zirconia Ceramic Thermal Barrier Coatings, *J. Phys. Chem. C*, 2014, **118**(25), p 13590-13597
5. L.A. Dombrovsky, H.K. Tagne, D. Baillis, and L. Gremillard, Near-Infrared Radiative Properties of Porous Zirconia Ceramics, *Infrared Phys. Technol.*, 2007, **51**(1), p 44-53
6. L. Wang, P. Zhang, M.H. Habibi, J.I. Eldridge, and S.M. Guo, Infrared Radiative Properties of Plasma-Sprayed Strontium Zirconate, *Mater. Lett.*, 2014, **137**, p 5-8
7. J. Marthe, E. Meillot, G. Jeandel, F. Enguehard, and J. Ilavsky, Enhancement of Scattering and Reflectance Properties of Plasma-Sprayed Alumina Coatings by Controlling the Porosity, *Surf. Coat. Technol.*, 2013, **220**, p 80-84
8. A. Hall, A. Ambrosini, and C.K. Ho, Solar Selective Coatings for Concentrating Solar Power Central Receivers, *Adv. Mater. Process.*, 2012, **170**(1), p 28-32
9. E. Brousse-Pereira, K. Wittmann-Ténèze, V. Bianchi, J.L. Longuet, and L. Del Campo, Optical and Electrical Properties of Heterogeneous Coatings Produced by Aluminum Powder and Boehmite Suspension Plasma Spraying, *J. Thermal Spray Technol.*, 2012, **21**(6), p 1110-1119
10. V. Debout, F. Enguehard, E. Meillot, A. Vardelle, P. Abelard, E. Bruneton, and P. Fauchais, Optical and Radiative Properties of YSZ Plasma-Sprayed Coatings, *Radiative Transfer—V. Proceedings of the Fifth International Symposium on Radiative Transfer*, 2007, Bodrum, Turkey, June 17-22
11. B.J. Zhang, B.X. Wang, and C.Y. Zhao, Microstructural Effect on the Radiative Properties of YSZ Thermal Barrier Coatings (TBCs), *Int. J. Heat Mass Transf.*, 2014, **73**, p 59-66
12. O. Rozenbaum, D. De Sousa Meneses, P. Echegut, and P. Levitz, Influence of the Texture on the Radiative Properties of Semitransparent Materials. Comparison Between Model and Experiment, *High Temp.: High Press.*, 2000, **32**(1), p 61-66
13. B. Rousseau, H. Gomart, D. De Sousa Meneses, P. Echegut, M. Rieu, R. Dugas, P. Lenormand, and F. Ansart, Modelling of the Radiative Properties of an Opaque Porous Ceramic Layer, *J. Electroceram.*, 2011, **27**, p 89-92
14. D. Toru, A. Quet, D. De Sousa Meneses, L. del Campo, and P. Echegut, Influence of Microstructure and Composition on Optical Properties of Plasma-Sprayed Al/Al$_2$O$_3$ Cermets, *J. Phys. Chem. C*, 2015, **119**(10), p 5426-5433
15. E. Palik, *Handbook of Optical Constant of Solids III*, Vol 3, Academic Press, New York, 1998, p 761-763
16. A.D. Rakic, Algorithm for the Determination of Intrinsic Optical Constants of Metal Films: Application to Aluminum, *Opt. Soc. Am.*, 1995, **34**, p 4755-4765
17. O. Rozenbaum, D. De Sousa Meneses, and P. Echegut, Texture and Porosity Effects on the Thermal Radiative Behavior of Alumina Ceramics, *Int. J. Thermophys.*, 2009, **9**, p 580-590
18. O. Ansellem, K. Madi, F. Borit, D. Jeulin, V. Guipont, M. Jeandin, E. Boller, and F. Pauchet, Three-Dimensional Simulation of Porosity in Plasma-Sprayed Alumina Using Microtomography and Electrochemical Impedance Spectrometry for Finite Element Modeling of Properties, *J. Thermal Spray Technol.*, 2012, **21**(2), p 193-201